Parameterization of Generalized Cloud Overlap for Radiative Calculations in General Circulation Models

WILLIAM D. COLLINS

National Center for Atmospheric Research, Boulder, Colorado*

(Manuscript received 12 September 2000, in final form 9 March 2001)

ABSTRACT

New radiative parameterizations have been developed for the National Center for Atmospheric Research (NCAR) Community Atmospheric Model (CAM). The CAM is the next version of the NCAR Community Climate Model (CCM). This paper describes the generalized treatment of vertical cloud overlap in the radiative calculations. The new parameterizations compute the shortwave and longwave fluxes and heating rates for random overlap, maximum overlap, or an arbitrary combination of maximum and random overlap. The specification of the type of overlap is identical for the two bands, and it is completely separated from the radiative parameterizations. In the prototype of CAM (CAM 0.1), adjacent cloud layers are maximally overlapped and groups of clouds separated by cloud-free layers are randomly overlapped. The introduction of the generalized overlap assumptions permits more realistic treatments of cloud–radiative interactions. The parameterizations are based upon representations of the radiative transfer equations that are more accurate than previous approximations. These techniques increase the computational cost of the radiative calculations by approximately 30%. The methodology has been designed and validated against calculations based upon the independent pixel approximation (IPA). The solution techniques and validation procedure are described in detail. The hourly radiative fluxes and heating rates from the parameterizations and IPA have been compared for a 1-yr integration of CAM. The mean and rms errors in the hourly longwave top of the atmosphere (TOA) fluxes are -0.006 ± 0.066 W m^{-2}, and the corresponding errors in the shortwave TOA fluxes are -0.20 ± 1.58 W m^{-2}. Heating rate errors are $O(10^{-3})$ K day^{-1}. In switching from random to maximum/random overlap, the largest changes in TOA shortwave fluxes occur over tropical continental areas, and the largest changes in TOA longwave fluxes occur in tropical convective regions. The effects on global climate are determined largely by the instantaneous changes in the fluxes rather than feedbacks related to cloud overlap.

1. Introduction

One of the challenges in studying the effects of clouds on climate is the uncertainty in the vertical distribution of cloud amount. To date, satellite and surface observations have provided only limited information on the vertical profiles of cloud cover (Haskins et al. 1995; Wang et al. 2000). The difficulties of treating complex cloud configurations in parameterizations of radiative transfer have been recognized for some time (Stephens 1984). The sensitivity of cloud precipitation and microphysics to the assumptions regarding cloud overlap has been identified more recently with the introduction of detailed schemes for cloud condensate (Jakob and Klein 1999, 2000). The focus of this paper is the treatment of vertical cloud overlap in the calculations of radiative fluxes and heating rates. The agreement between these calculations and observations depends on a number of factors, including the physical fidelity of the vertical cloud distributions and the accurate treatment of cloud and trace-gas optical properties. The common assumptions that clouds have plane-parallel geometry and internal homogeneity also limit the accuracy of simulated radiation fields (Barker 1996; Barker and Wielicki 1997). The variability in subgrid cloud structure introduces additional degrees of freedom (Stubenrauch et al. 1997), which are neglected in most climate models. The issues regarding the realism of the vertical cloud distributions, atmospheric optical properties, and simplified plane-parallel geometry have been discussed extensively and will not be examined further here. This study will address a more limited issue: Given a particular plane-parallel homogeneous cloud field and a specification of its vertical overlap, can the radiative effects of cloud overlap be calculated quickly and accurately in general circulation models (GCMs)?

In models with high spatial resolution, for example large-eddy simulations, individual cloud elements are

* The National Center for Atmospheric Research is supported by the National Science Foundation.

Corresponding author address: Dr. William D. Collins, National Center for Atmospheric Research, P.O. Box 3000, Boulder, CO 80307-3000.
E-mail: wcollins@ucar.edu

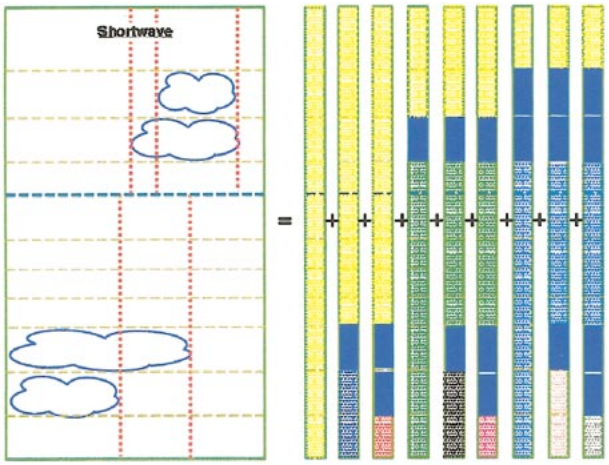

FIG. 1. An example of the conversion of a vertical profile of partial cloud amounts to an equivalent set of binary cloud configurations. The overlap is assumed to be M/R with M overlap between clouds in adjacent layers and R overlap between groups of clouds separated by clear sky. The stippled color coding of layers in the binary cloud configurations indicates which configurations share identical radiative properties for downwelling direct and diffuse shortwave radiation at a given layer. The solid blue regions are clouds.

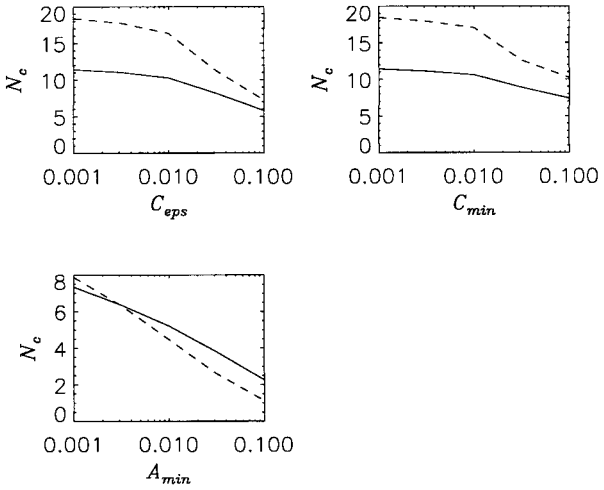

FIG. 2. Variation of the number of configurations N_c [Eq. (3)] with the parameters in Table 3 for accelerating the shortwave calculation: (a) C_{eps}, (b) C_{min}, and (c) $\tilde{A}_{\text{min}}$. Solid lines represent the mean value of N_c and dashed lines represent the rms value of N_c.

fully resolved on the model grid. In these models the atmosphere is a binary mixture of completely clear and cloud-filled elements so that no overlap assumptions are necessary. In GCMs, the vertical correlations between clouds have to be prescribed because cloud elements are much smaller than a typical GCM grid cell and because there is no general theory for how different cloud systems should overlap. In a recent intercomparison of GCMs (Phillips 1994), the most common overlap assumptions are random (Manabe and Strickler 1964), hereafter denoted by R; and maximum/random (Geleyn and Hollingsworth 1979), hereafter M/R. One type of M/R has maximum cloud overlap in each of three regions representing the lower, middle, and upper troposphere and random overlap between these regions (e.g., Chou et al. 1998). A second type of M/R has maximum overlap between clouds in adjacent levels and random overlap between groups of clouds separated by one or more clear layers (e.g., Zdunkowski et al. 1982). The latter form of M/R is the most consistent with a statistical analysis of observed cloud distributions (Tian and Curry 1989). Analysis of radar profiles of cloud cover in central England support the assumption of random overlap between clouds separated by clear sky (Hogan and Illingworth 2000). However, the maximum overlap between adjacent cloud-filled layers relaxes to random overlap with an *e*-folding distance of 1.5–3 km.

The climate simulated with GCMs can be quite sensitive to the assumptions regarding cloud overlap in the radiative calculations. The responses to variation in overlap can include significant changes in radiative heating rates, atmospheric temperature, hydrological processes, and daily variability (Liang and Wang 1997;

TABLE 1. Definition of symbols.

Symbol	Definition	Units
S(TOA)	TOA net all-sky shortwave flux (+ down)	W m^{-2}
S(0)	Surface net all-sky shortwave flux (+ down)	W m^{-2}
S_c(TOA)	TOA net clear-sky shortwave flux (+ down)	W m^{-2}
S_c(0)	Surface net clear-sky shortwave flux (+ down)	W m^{-2}
F(TOA)	TOA net all-sky longwave flux (+ up)	W m^{-2}
F(0)	Surface net all-sky longwave flux (+ up)	W m^{-2}
F_c(TOA)	TOA net clear-sky longwave flux (+ up)	W m^{-2}
F_c(0)	Surface net clear-sky longwave flux (+ up)	W m^{-2}
Q_{SW}	Shortwave all-sky heating rate	K day^{-1}
Q_{LW}	Longwave all-sky heating rate	K day^{-1}
C_L	M/R cloud amount, 700 mb to surface	—
C_M	M/R cloud amount, 400 to 700 mb	—
C_H	M/R cloud amount, TOA to 400 mb	—
C_T	Total M/R cloud amount	—
P_L	Area-mean liquid water path	g m^{-2}
P_I	Area-mean ice water path	g m^{-2}

TABLE 2. Definition of terms in fluxes.

Term	Definition
σ	Stefan–Boltzmann constant
p	Pressure
$p_t(i)$	Pressure at top of layer i
$p_b(i)$	Pressure at bottom of layer i ($p_b(i) > p_t$(i))
$T(p)$	Temperature at pressure p
$B(p)$	$\sigma T^4(p)$
$i^{\downarrow}_{p,j}$	Layer containing pseudocloud for $\bar{F}^{\downarrow}(i_{j,\min})$ boundary condition
$i^{\uparrow}_{p,j}$	Layer containing pseudocloud for $\bar{F}^{\uparrow}(i_{j,\max})$ boundary condition
$\epsilon(i)$	Emissivity of cloud in layer i
$\epsilon_{p,j}(i)$	Emissivity of pseudoclouds at $i = i^{\downarrow}_{p,j}$ and $i^{\uparrow}_{p,j}$
$\alpha(p, p')$	Clear-sky emissivity from pressure p' to p (Kiehl et al., 1996)
$F^{\downarrow}_{\text{clr}}(i)$	Downwelling clear-sky flux at layer i (Kiehl et al., 1996)
$F^{\uparrow}_{\text{clr}}(i)$	Upwelling clear-sky flux at layer i (Kiehl et al., 1996)
$t^{\uparrow\downarrow}_{j,k}(i)$	Weights for up-/downwelling clear-sky flux at layer i
$T^{\uparrow\downarrow}_{j,kj}(i, i')$	Weights for up-/downwelling flux at layer i from cloud at i'

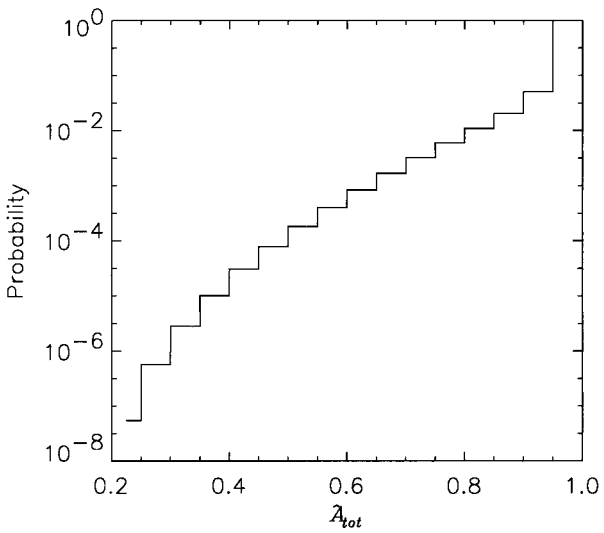

FIG. 3. Cumulative probability of the fractional area $\tilde{A}_{\text{tot}}$ [Eq. (15)] of cloud configurations included in the shortwave calculations based upon the shortwave acceleration parameters (Table 3). Statistics are accumulated each hour from a global 1-yr integration.

Morcrette and Jakob 2000). The surface fluxes are also quite sensitive to the type of cloud overlap (Morcrette and Jakob 2000). Therefore the overlap assumption can affect the exchange of energy between the atmosphere and other components of a coupled climate model, but the sensitivity of coupled models to cloud overlap has not been systematically explored.

Accurate treatment of cloud overlap can significantly increase the complexity and computational cost of radiative parameterizations. This is especially true in the shortwave since the interaction between upwelling and downwelling radiation is nonlinear due to multiple scattering. For these reasons, nearly all existing treatments of cloud overlap are approximate. In the method of Geleyn and Hollingsworth (1979), the all-sky fluxes are estimated by weighting clear-sky and cloudy-sky fluxes with functions of cloud amount. This approach assumes that radiative processes in the clear and cloudy regions of a model layer produce horizontally uniform outgoing fluxes from horizontally inhomogeneous incoming fluxes. Variants of this approach have been widely adopted (Hense et al. 1982; Geleyn et al. 1982; Zdunkowski et al. 1982; Morcrette and Geleyn 1985). In the model of Harshvardhan et al. (1987), the all-sky longwave flux at each layer interface includes a weighted sum of the blackbody emissions from clouds. The weights are the fractional areas of each cloud that are not obstructed by other clouds closer to the given interface (Washington and Williamson 1977). This method has been modified by Raisanen (1998) to remove a spurious dependence on vertical resolution, but the modified approach is still approximate. For shortwave calculations, Lacis and Hansen (1974) treat cloud overlap using an effective optical depth for each layer that depends on cloud amount. Similar techniques have been developed by Harshvardhan et al. (1987), Briegleb (1992), Stubenrauch et al. (1997), and Chou et al. (1998). Fouquart and Bonnel (1980) parameterize cloud overlap by deriving effective reflection and transmission functions for all-sky conditions. These functions are linear combinations of the corresponding functions for clear and overcast conditions with weights that depend on cloud amount. This method has been developed further by Morcrette and Fouquart (1986), Bergman and Hendon (1998), and Morcrette and Jakob (2000). In general, the errors introduced by these approximations have been estimated using a rather limited set of benchmark calculations.

In this paper we describe a new set of parameterizations of cloud overlap for calculations of radiative transfer suitable for use in GCMs. The GCM [the National Center for Atmospheric Research (NCAR) prototype Community Atmospheric Model (CAM 0.1)] used to test the parameterizations is described in section 2. The methods used to implement the overlap, the options available to reduce the execution time of these methods, and the particular overlap assumption adopted in CAM are described in section 3. The parameterizations are designed to reproduce calculations using the independent pixel approximation (IPA). The evaluation of the new methods against IPA is discussed in section

TABLE 3. Parameters for decreasing number of SW calculations.

Parameter	Symbol	Definition	Value*
cldmin	$C_{\min}$	Minimum cloud area	0
cldeps	C_{eps}	Minimum cloud area difference	0
areamin	$A_{\min}$	Minimum configuration area	0.01
nconfgmax	$N_{c,\max}$	Maximum no. of configurations	15

* CAM 0.1.

4. The response of the climate simulated by CAM to changes in cloud overlap is examined in section 5. The computational cost of the new radiative transfer codes relative to the random-overlap codes used in NCAR's Community Climate Model 3 (CCM3) is presented in section 6, and conclusions and future work are outlined in section 7.

2. Description of the CAM

The atmospheric model is the NCAR Community Atmospheric Model (CAM), formerly known at the Community Climate Model (CCM). Two versions are compared in this study, the CCM3 (Kiehl et al. 1996, 1998a) and a prototype of CAM. The characteristics of the climate simulated by CCM3 are described in Kiehl et al. (1998b), Hack et al. (1998), and Hurrell et al. (1998). There are several major differences in the model physics and structure between CCM3 and CAM aside from the generalization in cloud overlap. First, the distribution and evolution of cloud water is treated with a prognostic parameterization (Rasch and Kristjánsson 1998) in place of the diagnostic prescription used in CCM3 (Hack 1998). Second, the default vertical discretization is set to 30 levels rather than 18 levels. The increased resolution will facilitate the development of new parameterizations of the planetary boundary layer and boundary layer clouds. Third, the model has been generalized to accommodate a variety of dynamical cores, including the standard spectral Eulerian method (Williamson et al. 1987), semi-Lagrangian transport (Williamson and Rasch 1989), reduced grid calculations (Williamson and Rosinski 2000), and a flux-form semi-Lagrangian approach (Lin and Rood 1996, 1997). Fourth, the physical parameterizations have been completely separated from the dynamical cores to facilitate the introduction of new physics packages and dynamics in the model (Williamson 1999). Finally, the Zhang and McFarlane (1995) convective scheme in CCM3 (Zhang et al. 1998) will be modified in CAM. Although several convective parameterizations are under consideration, all the simulations discussed in this paper are based upon the scheme by Zhang and McFarlane (1995). In addition, all the simulations with the prototype are executed with the spectral Eulerian dynamics.

3. Method for solution

a. Overview

The basic fields computed by the radiative parameterizations include the shortwave and longwave heating rates and the all-sky fluxes at the surface. The heating rates are used to compute the temperature tendencies in the atmosphere, and the surface fluxes are used to compute the exchange of energy with other components of the climate system. The symbols for these fields and other diagnostic quantities are defined in Table 1. In CAM, the radiation time step is usually different from the time step for the dynamics. In the standard T42 configuration, the radiative heating rates and fluxes are computed once per hour at each grid point using the instantaneous atmospheric state at that time step. Although the CAM includes a provision to execute the radiation on a different vertical grid from that used in the dynamics, in the standard configuration the two vertical grids are identical.

Other than the generalization in cloud overlap, the radiative parameterizations in CAM are very similar to those in CCM3. The sets of optically active trace gases, the radiative properties of these gases, and the specification of cloud optical properties are identical to CCM3 (Kiehl et al. 1996). The shortwave scheme is based upon the δ-Eddington solution (Briegleb 1992), and the longwave scheme is still based upon the absorptivity–emissivity formulation of the equations for infrared radiation (Ramanathan and Downey 1986). In the standard configuration of CAM, the absorptivity and emissivity arrays are updated once every 12 h. This practice was first introduced in CCM in order to reduce the execution time, because the calculation of these arrays is the dominant computational cost for the entire longwave parameterization. The developers of CAM hope to implement a longwave scheme based upon the correlated-k technique (e.g., Lacis and Oinas 1991) in the next version of the model. However, careful study of several widely used versions of the correlated-k method has not identified a single implementation that is sufficiently robust, general, and efficient for use in CAM. Possible improvements in the treatment of infrared absorption by water vapor within the absorptivity–emissivity framework are discussed in section 7.

The new parameterizations can treat random, maximum, or an arbitrary combination of maximum and random overlap between clouds. The type of overlap is specified with the same two variables for the longwave and shortwave calculations. These variables are the number of random-overlap interfaces between adjacent groups of maximally overlapped layers and a vector of the pressures at each of the interfaces. To implement pure random overlap, the number of interfaces would equal the number of model levels, and the vector of pressures would equal the pressures at the bottom of each level. To implement pure maximum overlap, the number of interfaces would equal 1, and the pressure at that interface would be set to a value larger than the surface pressure. The version of M/R with maximum overlap in the lower, middle, and upper troposphere (e.g., Chou et al. 1998) is equivalent to setting the number of interfaces to 3 and the interface pressures to the pressures at the lower boundaries of the three regions. The specification of the overlap is completely separated from the radiative calculations, and if necessary the type of overlap can change at each grid cell or time step.

b. Longwave fluxes

If longwave scattering is omitted, the upwelling and downwelling longwave fluxes are solutions to uncoupled ordinary differential equations (Goody and Yung 1989). The emission from clouds is calculated using the Stefan–Boltzmann law applied to the temperatures at the cloud boundaries. The cloud boundaries correspond to the interfaces of the model layers. This approximation greatly simplifies the mathematical form of the flux solutions since the clouds can be treated as boundary conditions for the differential equations. The approximation becomes more accurate as the clouds become more optically thick. The clouds in CAM are graybodies with emissivities that depend on cloud phase, condensed water path, and the effective radius of ice particles (Kiehl et al. 1996). Many GCMs incorporate the same set of approximations in the context of the absorptivity–emissivity method. In virtually all these models, the longwave equations are solved using the cloud-overlap matrix method first proposed by Manabe and Strickler (1964). This method is not exact, and several modifications have been suggested to improve its accuracy (Raisanen 1998; Li 2000). However, it is possible to solve the set of radiative transfer equations exactly, and the method adopted in CAM is based upon the exact solution.

The algorithm for cloud overlap first converts the vertical profile of partial cloudiness into an equivalent collection of binary cloud configurations. Let $C(i)$ be the fractional amount of cloud in layer i in a profile with N layers. The index $i = 1$ corresponds to the top of the model atmosphere and $i = N$ corresponds to the layer adjacent to the surface. Let N_m be the number of maximally overlapped regions in the column separated by random-overlap boundaries. If the entire column is maximally overlapped, then $N_m = 1$, and if the entire column is randomly overlapped, then $N_m = N$. Each region j includes all layers i between $i_{j,\min}$ and $i_{j,\max}$. Within each region, identify the n_j unique, nonzero cloud amounts and sort them into a descending list C_{j,k_j} with $1 \le k_j \le n_j$. Note that in CAM, cloud amounts are not allowed to be identically equal to 1. It is convenient to define $C_{j,0} = 1$ and $C_{j,n_j+1} = 0$. By construction $C_{j,k_j-1} > C_{j,k_j}$ for $1 \le k_j \le n_j + 1$.

The binary cloud configurations are defined in terms of the sorted cloud amounts. The number of unique cloud binary configurations in region j is $n_j + 1$. The k_jth binary cloud configuration $\tilde{C}_{j,k_j}$ in region j is given by

$$\tilde{C}_{j,k_j}(i) = \begin{cases} 1 & \text{if } i_{j,\min} \le i \le i_{j,\max} \quad \text{and} \quad C(i) \ge C_{j,k_j-1} \\ 0 & \text{otherwise,} \end{cases} \tag{1}$$

with $1 \le k_j \le n_j + 1$. The fractional area of this configuration is

$$\tilde{A}_{j,k_j} = C_{j,k_j-1} - C_{j,k_j}. \tag{2}$$

The binary cloud configurations for each maximum-overlap region can be combined into cloud configurations for the entire column. Because of the random-overlap boundaries between regions, the number of column configurations is

$$N_c = \prod_{j'=1}^{N_m} (n_{j'} + 1). \tag{3}$$

Let $\tilde{C}[k_1, \ldots, k_{N_m}]$ represent the column configuration with $\tilde{C}_{1,k_1}$ in region 1, $\tilde{C}_{2,k_2}$ in region 2, etc. The vertical profile of binary cloud elements is given by

$$\tilde{C}[k_1, \ldots, k_{N_m}](i) = \sum_{j'=1}^{N_m} \tilde{C}_{j',k_{j'}}(i). \tag{4}$$

The area of this configuration is

$$\tilde{A}[k_1, \ldots, k_{N_m}] = \prod_{j'=1}^{N_m} \tilde{A}_{j',k_{j'}}. \tag{5}$$

First consider the flux boundary conditions for a maximum-overlap region j. The downward flux at the upper boundary of the region is spatially heterogeneous and has terms contributed by all the binary configurations above the region. Similarly, the upward flux at the lower boundary of the region has terms contributed by all the binary configurations below the region. The fluxes within the region are area-weighted sums of the fluxes calculated for all possible combinations of these boundary terms and the cloud configurations within the region. Fortunately, the arithmetic can be simplified because the solutions to the longwave equations are linear in the boundary conditions. Therefore the downward (upward) fluxes can be computed by summing the solutions for each configuration in the region for a single boundary condition given by $\overline{F}^{\downarrow}(i_{j,\min})$ [$\overline{F}^{\uparrow}(i_{j,\max})$]. This is explained in the appendix. In the absorptivity–emissivity method, the boundary conditions are included in the solution using the emissivity array. In the standard formulation (Manabe and Möller 1961; Ramanathan and Downey 1986) used in CAM, this array is only defined for boundary conditions at the top of the model domain for computational economy. It is not possible to treat arbitrary flux boundary conditions inside the domain [(e.g., $\overline{F}^{\downarrow}(i_{j,\min})$] using the emissivity array. However, the flux boundary conditions $\overline{F}^{\downarrow}(i_{j,\min})$ and $\overline{F}^{\uparrow}(i_{j,\max})$ are mathematically equivalent to the fluxes from a single ''pseudo'' cloud deck above and below the region, respectively. The pseudoclouds have unit area and occupy a single model layer. The vertical positions and emissivities of these clouds are chosen so that the net area-mean fluxes incident on the top and bottom of the region equal $\overline{F}^{\downarrow}(i_{j,\min})$ and $\overline{F}^{\uparrow}(i_{j,\max})$. With the introduction of the pseudoclouds, the fluxes inside each maximum-overlap region can be calculated using the standard absorptivity–emissivity formulation.

The total upward and downward mean fluxes at a

layer i within a maximum-overlap region j are given by

$$\overline{F}^{\uparrow}(i) = \sum_{k_j=1}^{n_j+1} \tilde{A}_{j,k_j} \overline{F}[k_j]^{\uparrow}(i)$$

$$\overline{F}^{\downarrow}(i) = \sum_{k_j=1}^{n_j+1} \tilde{A}_{j,k_j} \overline{F}[k_j]^{\downarrow}(i), \tag{6}$$

where $\overline{F}[k_j]^{\uparrow}(i)$ and $\overline{F}[k_j]^{\downarrow}(i)$ are the upward and downwelling fluxes for the cloud configuration $\tilde{C}_{j,k_j}$. The symbols required to write these fluxes are defined in Table 2. The downward and upward fluxes for each configuration can be derived by iterating the longwave equations from TOA and the surface to the layer i. At each iteration, the solutions are advanced between successive cloud layers. The final form of the fluxes in configuration $\tilde{C}_{j,k_j}$ is

$$\overline{F}[k_j]^{\uparrow}(i) = F^{\uparrow}_{\mathrm{clr}}(i) t^{\uparrow}_{j,k_j}(i) + \sum_{i'=i}^{N} \left\{ B[p_t(i')] - \int_{p_t(i)}^{p_t(i')} \alpha[p_t(i), p'] \frac{dB(p')}{dp'}\, dp' \right\} T^{\uparrow}_{j,k_j}(i, i') \tag{7}$$

$$\overline{F}[k_j]^{\downarrow}(i) = F^{\downarrow}_{\mathrm{clr}}(i) t^{\downarrow}_{j,k_j}(i) + \sum_{i'=1}^{i} \left\{ B[p_b(i')] + \int_{p_b(i')}^{p_b(i)} \alpha[p_b(i), p'] \frac{dB(p')}{dp'}\, dp' \right\} T^{\downarrow}_{j,k_j}(i, i'). \tag{8}$$

The clear-sky and cloudy-sky weights are

$$t^{\uparrow}_{j,k_j}(i) = \prod_{l=i}^{N} [1 - \tilde{\epsilon}_{j,k_j}(l)] \tag{9}$$

$$t^{\downarrow}_{j,k_j}(i) = \prod_{l=1}^{i} [1 - \tilde{\epsilon}_{j,k_j}(l)] \tag{10}$$

$$T^{\uparrow}_{j,k_j}(i, i') = \tilde{\epsilon}_{j,k_j}(i') \prod_{l=i}^{i'-1} [1 - \tilde{\epsilon}_{j,k_j}(l)] \tag{11}$$

$$T^{\downarrow}_{j,k_j}(i, i') = \tilde{\epsilon}_{j,k_j}(i') \prod_{l=i'+1}^{i} [1 - \tilde{\epsilon}_{j,k_j}(l)] \tag{12}$$

$$\tilde{\epsilon}_{j,k_j}(l) = \begin{cases} \epsilon(l) \tilde{C}_{j,k_j}(l) & \text{if } i_{j,\min} \le l \le i_{j,\max} \\ \epsilon_{p,j}(i^{\downarrow}_{p,j}) & \text{if } l = i^{\downarrow}_{p,j} \\ \epsilon_{p,j}(i^{\uparrow}_{p,j}) & \text{if } l = i^{\uparrow}_{p,j} \\ 0 & \text{otherwise.} \end{cases} \tag{13}$$

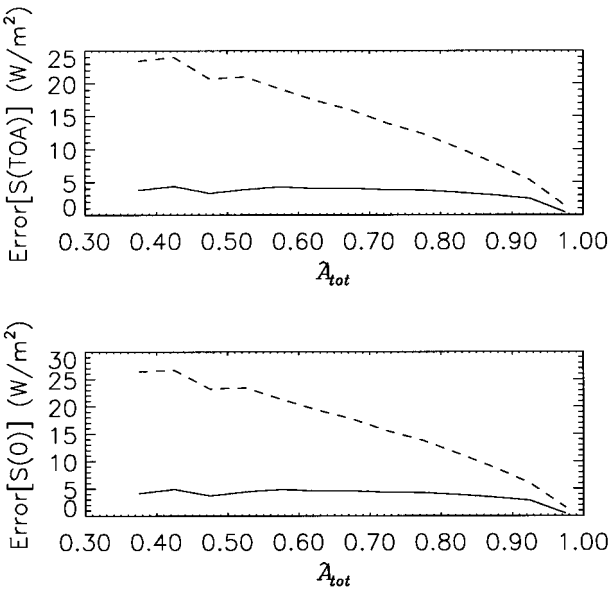

FIG. 4. Variation of instantaneous mean and rms errors in all-sky fluxes with $\tilde{A}_{\mathrm{tot}}$ [Eq. (15)]: (a) S(TOA), (b) S(0). Solid lines are mean errors and dashed lines are rms errors in the fluxes. Statistics are obtained from a global 1-yr integration.

c. Shortwave fluxes

The solution for the shortwave fluxes is calculated by determining all possible arrangements of binary clouds that are consistent with the vertical profile of partial cloudiness and the overlap assumption. This process is illustrated in Fig. 1. The shortwave radiation within each of these configurations is calculated using the same δ-Eddington solver introduced in CCM3 (Briegleb 1992). The all-sky fluxes and heating rates for the original profile of partial cloudiness are calculated as weighted sums of the corresponding quantities from each configuration. The weights are equal to the horizontal fractional area occupied by each configuration. The number of configurations is given by Eq. (3), and the area of each configuration is given by Eq. (5). There are two steps in the calculations: first, the calculation of the cloud-free and overcast radiative properties for each layer, and second, the combination of these properties using the adding method to calculate fluxes.

This method has long been recognized as the most accurate technique for treating overlap between plane-parallel clouds in shortwave calculations, although it is frequently asserted to be the most computationally expensive (Fouquart 1988; Chou et al. 1998). However, as shown in section 6, the computational cost for the present method applied to M/R overlap is quite competitive with existing less-accurate approximations. One reason for the computational efficiency of the new scheme is the elimination of duplicative calculations.

TABLE 4. Difference between fields for maximum/random and random overlap.

Field[a]	M/R int. − R int.[b]	M/R int.	M/R int. − R diag.[c]	M/R diag. − R int.[d]
S(TOA)	1.68	235.80	1.56	1.49
S(0)	1.34	170.28	1.32	1.25
S_c(TOA)	0.19	283.28	0.16	0.16
S_c(0)	−0.36	221.06	−0.26	−0.26
F(TOA)	0.98	235.83	0.41	0.43
F(0)	1.75	62.54	2.01	2.17
F_c(TOA)	−0.86	265.35	0.00	0.00
F_c(0)	−0.55	93.64	0.00	0.00
C_L	−0.001	0.443	—	—
C_M	−0.002	0.202	—	—
C_H	−0.003	0.405	—	—
C_T	−0.004	0.663	—	—
P_L	0.05	38.43	—	—
P_I	−0.11	8.56	—	—

[a] Units are defined in Table 1.
[b] Total change in fields switching from R to M/R overlap (codes are interactive).
[c] New codes with M/R overlap are interactive and the old codes with R overlap are diagnostic.
[d] Old codes with R overlap are interactive and new codes with M/R overlap are diagnostic.

To compute the fluxes at an interface, the scheme requires five bulk radiative properties (Briegleb 1992):

T_{dir} = transmission of direct beam from top of the atmosphere (TOA) to interface,
$\underline{T}_{\text{dn}}$ = total transmission from TOA to interface,
$\overline{R}_{\text{dn}}$ = reflectivity of atmosphere above interface to upwelling diffuse radiation,
R_{up} = reflectivity of surface–atmosphere system below interface to downwelling direct radation, and
$\overline{R}_{\text{up}}$ = reflectivity of surface–atmosphere system below interface to downwelling diffuse radation.

Here, T_{dir}, T_{dn}, and $\overline{R}_{\text{dn}}$ are calculated using the adding method applied to the radiative properties of each layer starting at TOA and continuing down to the interface. If two or more configurations of binary clouds are identical between TOA and a particular interface, then T_{dir}, T_{dn}, and $\overline{R}_{\text{dn}}$ are also identical at that interface. The adding method is applied once and the three radiative quantities are copied to all the identical configurations. This process is applied at each interface by constructing a binary tree of identical cloud configurations starting at TOA down to the surface. An illustration of this approach is shown in Fig. 1. A similar method is used for R_{up} and $\overline{R}_{\text{up}}$, which are calculated using the adding method starting at the surface and continuing up to a particular interface. The copying of identical radiative properties reduces the number of calculations of T_{dir}, T_{dn}, and $\overline{R}_{\text{dn}}$ by 62% and the number of calculations of R_{up} and $\overline{R}_{\text{up}}$ by 21% in CAM with M/R overlap.

The correct formulation of the adding method involves additional terms that are analogous to the terms defined above but are calculated from the interface to the TOA and surface (Hunt 1971). The new shortwave scheme retains the simplification introduced in CCM3 of approximating these additional terms with the corresponding terms calculated from the column boundaries to the interface. This simplification eliminates doubling the execution cost of the adding method. The relative errors in S(TOA) introduced by this approximation are $\leq$0.1%.

The computational cost of the shortwave code has two components: a fixed cost for computing the radiative properties of each layer under clear and overcast conditions, and a variable cost for applying the adding method for each column configuration $\tilde{C}[k_1, \ldots, k_{N_m}]$. The variable component can be reduced by omitting configurations that contribute small terms in the shortwave fluxes. Several mechanisms for selecting configurations for omission have been included in the parameterization. The parameters in CAM 0.1 that govern the selection process are described in Table 3. Any combination of the selection conditions may be imposed. If the parameter $C_{\text{min}} > 0$, cloud layers with $C(i) \leq C_{\text{min}}$ are identified as cloud-free layers. The configurations including these clouds are excluded from the flux calculations. If the parameter $C_{\text{eps}} > 0$, the cloud amounts are discretized by

$$C(i) \rightarrow \left[\frac{C(i)}{C_{\text{eps}}}\right] C_{\text{eps}}, \tag{14}$$

where $[x]$ represents rounding to the nearest integer less than x. This reduces the number of unique, nonzero cloud amounts n_j in each maximum-overlap region j. For example, if $C_{\text{eps}} = 0.01$, then two cloud amounts are distinguished only if they differ by more than 0.01. If the parameter $\tilde{A}_{\text{min}} > 0$, only configurations with $\tilde{A}[k_1, \ldots, k_{N_m}] \geq \tilde{A}_{\text{min}}$ are retained in the calculation. The

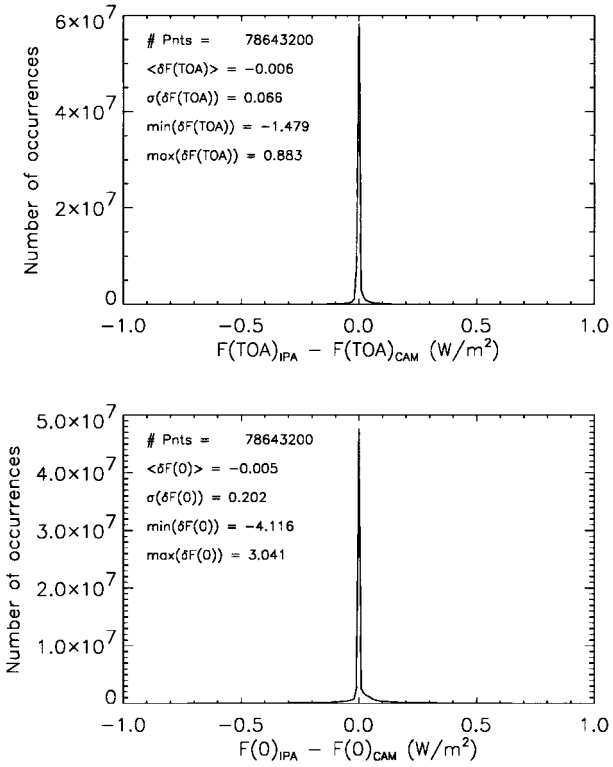

FIG. 5. (a) Distribution of differences in instantaneous TOA all-sky longwave fluxes F(TOA) from the IPA and CAM radiation codes. (b) Distribution of differences in instantaneous surface all-sky longwave fluxes $F(0)$. The differences are accumulated from a 1-yr integration of CAM at T42 resolution. The fluxes are computed at each radiation time step (1 h^{-1}) at each grid point. The statistics shown in each panel are, from top to bottom, the number of points in the distribution and the mean, rms, minimum, and maximum differences in instantaneous fluxes (IPA − CAM).

fluxes and heating rates are normalized by the area of these configurations:

$$\tilde{A}_{\text{tot}} = \sum_{k_1=1}^{n_1+1} \cdots \sum_{k_{N_m}=1}^{n_{N_m}+1} \tilde{A}[k_1, \ldots, k_{N_m}] \times \theta(\tilde{A}[k_1, \ldots, k_{N_m}] - \tilde{A}_{\text{min}}), \quad (15)$$

where θ is the Heaviside function. In CAM 0.1, $\tilde{A}_{\text{min}} = 0.01$. The variation of the number of configurations N_c for M/R overlap with each of the parameters is shown in Fig. 2. Finally, if the number of configurations $N_c > N_{c,\text{max}}$, then only the $N_{c,\text{max}}$ configurations with the largest values of $\tilde{A}[k_1, \ldots, k_{N_m}]$ are retained. This is equivalent to setting $\tilde{A}_{\text{min}}$ so that the largest $N_{c,\text{max}}$ configurations are selected. The fluxes and heating rates are normalized by $\tilde{A}_{\text{tot}}$ calculated with this value of $\tilde{A}_{\text{min}}$. With the current cloud parameterizations in CAM 0.1 and with $\tilde{A}_{\text{min}} = 0.01$, the mean and rms N_c are approximately 5. The value of $N_{c,\text{max}}$ is set to 15, or two standard deviations above the mean N_c. Only 5% of cloud configurations in CAM have $N_c \geq N_{c,\text{max}}$.

The cumulative probability distribution of $\tilde{A}_{\text{tot}}$ with the current set of shortwave acceleration parameters (Table 3) is plotted in Fig. 3. Approximately 95% of the shortwave calculations have $\tilde{A}_{\text{tot}} \geq 0.95$. The errors in the shortwave fluxes due to the omission of cloud configurations should increase with decreasing $\tilde{A}_{\text{tot}}$. As $\tilde{A}_{\text{tot}}$ decreases, the fluxes are being estimated from a progressively smaller area of the cloud field that may not be representative of the clouds in the rest of the grid box. The variation of the instantaneous mean and rms errors in $S(0)$ and S(TOA) with $\tilde{A}_{\text{tot}}$ is shown in Fig. 4. The mean and rms errors do not exceed 5 and 30 W m^{-2}, respectively, for $\tilde{A}_{\text{tot}} \geq 0.35$. Although the statistical sample is not adequate to compute the flux errors for $\tilde{A}_{\text{tot}} < 0.35$, Fig. 3 shows there is no significant trend in the errors at small values of $\tilde{A}_{\text{tot}}$.

d. Overlap assumption for CAM

The cloud overlap for radiative calculations in CAM 0.1 is M/R. Clouds in adjacent layers are maximally overlapped, and groups of clouds separated by one or more clear layers are randomly overlapped. This type of M/R was first introduced by Geleyn and Hollingsworth (1979) and has been widely adopted (e.g., Zdunkowski et al. 1982; Stubenrauch et al. 1997). The M/R

TABLE 5. Increase in CAM execution time with new overlap.

Processors*	Increase**
8	1.19
16	1.15
32	1.22

* The system is an IBM SP2. Each processor is a 64-bit 375-MHz POWER3 CPU. Four processors compose an RS/6000 node.

** Ratio of the wall clock execution times for prototype CAM run with the new and old radiation schemes for a 2-day integration.

TABLE 6. Increase in radiation execution time with new overlap.

Band	Increase*
Shortwave	2.14
Longwave	1.03
Both	1.31

* Ratio of the wall clock execution times for new and old radiation schemes running in prototype CAM on 32 IBM SP2 processors for 2-day integration.

TABLE 7. Load balance of old and new radiation schemes.

Band	Old*	New**
Shortwave	1.91	2.69
Longwave	1.04	1.05

* Ratio of the maximum-to-mean wall clock execution times on individual processors for old radiation code running in prototype CAM. Statistics are from a 2-day integration on 32 processors of an IBM SP2.

** Ratio of the maximum-to-mean wall clock execution times on individual processors for new radiation code.

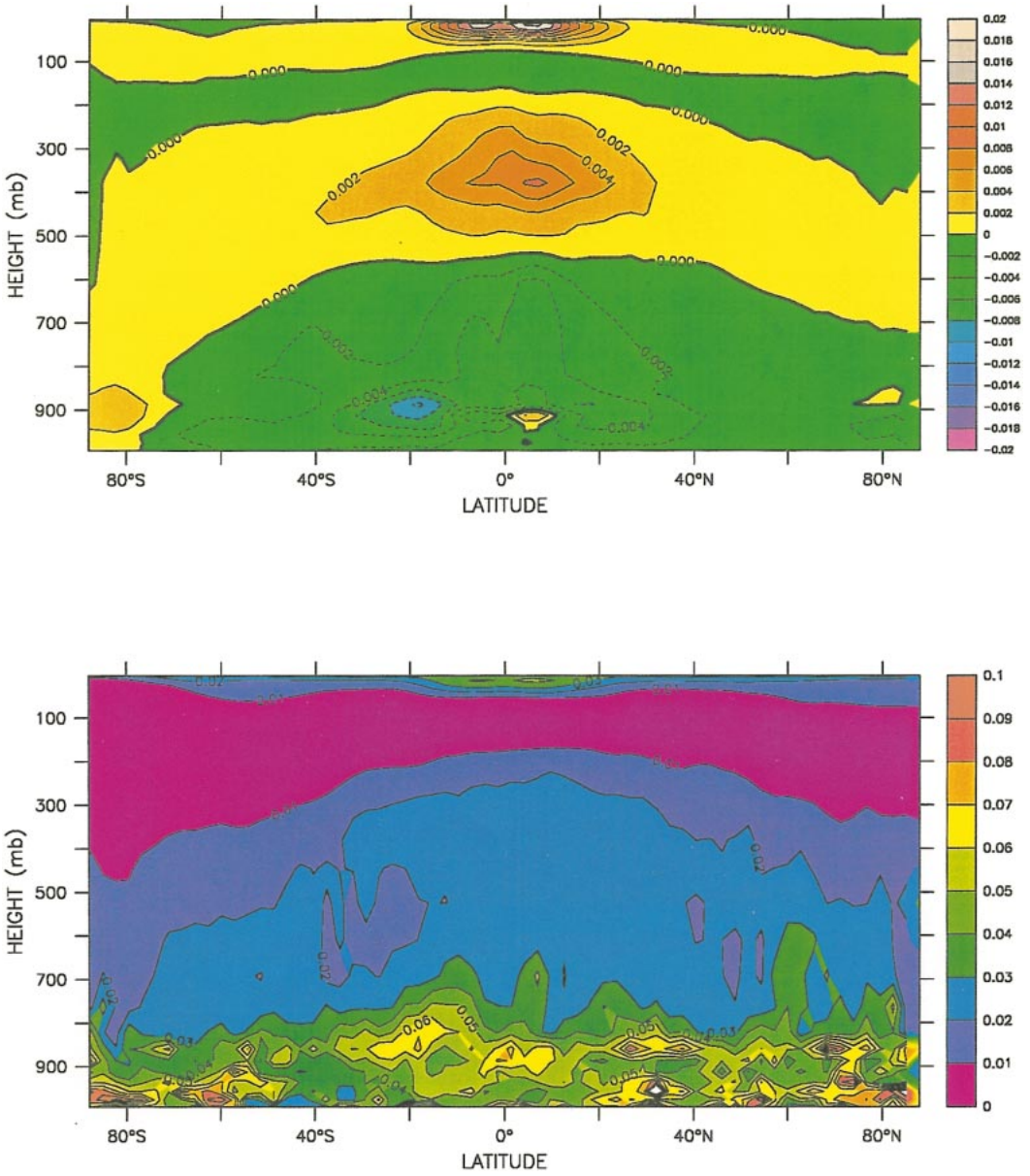

FIG. 6. (a) Zonally averaged mean differences in instantaneous longwave heat rates Q_{LW} from the IPA and CAM radiation codes; (b) zonally averaged rms differences in instantaneous longwave heat rates Q_{LW}. The differences are accumulated from a 1-yr integration of CAM at T42 resolution. The heating rates are computed at each radiation time step (1 h^{-1}) at each grid point.

overlap assumption has some observational support and is more consistent with estimates of total cloud cover (Tian and Curry 1989), although radar data indicate that the maximum overlap between adjacent clouds may relax to random overlap over vertical distances of 1.5–3 km (Hogan and Illingworth 2000).

The vertical cloud amount in each grid cell is determined from the same cloud parameterizations used in earlier versions of CCM (Hack 1998; Kiehl et al. 1998a). The clouds in adjacent layers are maximally overlapped, and groups of vertically contiguous clouds separated by clear layers are randomly overlapped. The two overlap parameters input to the radiative calculations are the number of random-overlap interfaces, which equals N_m, and a vector of pressures $\mathbf{p}$ at each random-overlap interface. These parameters are determined for each grid cell at each radiation time step. Suppose there are $M \geq 0$ groups of vertically contiguous clouds in a given grid cell. The first parameter $N_m = \max(M, 1)$. Let p_j represent the pressure at the bottom interface of each group

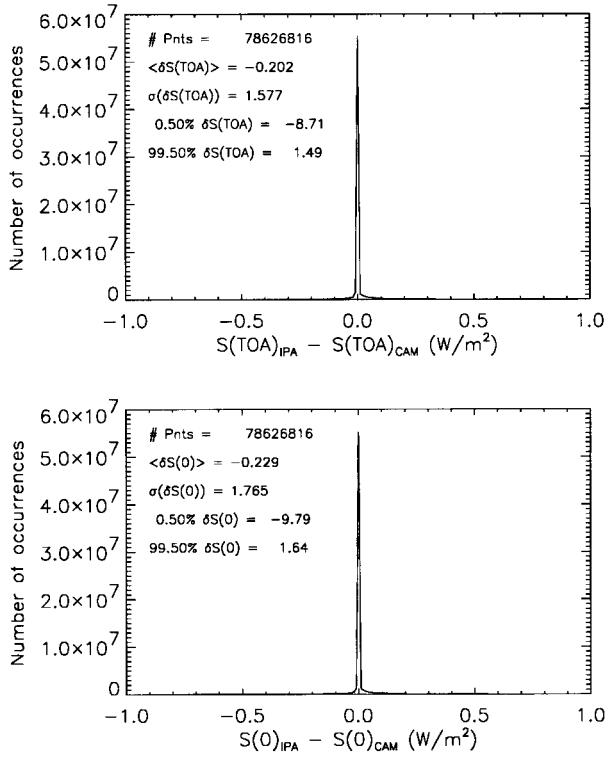

FIG. 7. (a) Distribution of differences in instantaneous TOA all-sky shortwave fluxes S(TOA) from the IPA and CAM radiation codes; (b) distribution of differences in instantaneous surface all-sky shortwave fluxes $S(0)$. The differences are accumulated from a 1-yr integration of CAM at T42 resolution. The fluxes are computed at each radiation time step (1 h^{-1}) at each grid point. The statistics shown in each panel are, from top to bottom, the number of points in the distribution and the mean, rms, 0.5 percentile, and 99.5 percentile differences in instantaneous fluxes (IPA − CAM).

of contiguous clouds, and let p_s denote the surface pressure. Both j and p_j increase from the top of the model downward. Then,

$$\mathbf{p} = \begin{cases} [p_s] & \text{if } M \leq 1 \\ [p_1, \ldots, p_{M-1}, p_s] & \text{if } M \geq 2. \end{cases} \quad (16)$$

It should be emphasized that the overlap assumption may be different in the first public release of CAM and that CAM can readily be executed with other types of cloud overlap. It should also be noted that the prognostic cloud-condensate parameterization (Rasch and Kristjánsson 1998) is based upon the maximum-overlap assumption. In the present version of the cloud-condensate scheme, this overlap assumption cannot be varied, and it may therefore be inconsistent with the overlap adopted in the radiation calculations. The experiments in section 5 are similar to the experiments by Morcrette and Jakob (2000) in which the overlap for radiation is varied independently of the overlap for the cloud condensate.

4. Evaluation against the independent pixel approximation

The accuracy of the new codes has been evaluated by comparison against calculations based upon the independent pixel approximation (IPA). This test quantifies the accuracy of the cloud overlap schemes relative to exact calculations for plane-parallel homogeneous clouds. In the IPA code, the input vertical cloud profile is converted into an equivalent set of binary cloud profiles. This process is similar to that used in the new shortwave code (section 3c). The fluxes and heating rates for each binary profile are calculated using the CCM3 radiation codes. Although the CCM3 codes are based upon the assumption of random overlap, the fluxes are computed correctly for binary clouds. The fluxes and heating rates for the original cloud profile are derived as weighted sums of corresponding quantities for each binary cloud configuration. The weights are the fractional surface areas occupied by each configuration. The radiative properties for trace gases and the optical properties for clouds are identical in the new codes and the IPA. The approximate two-stream methods for solving the radiative transfer equations are also identical. The comparison of the new codes against IPA can only identify errors associated with the approximations used to treat cloud overlap for plane-parallel clouds. The error estimates do not include the omission of three-dimensional subgrid cloud geometry from the calculation of fluxes and heating rates. However, the IPA yields accurate area-mean fluxes for complex arrangements of broken clouds (Cahalan et al. 1994; Zuidema and Evans 1998) and should therefore be suitable as a benchmark for comparison.

In order to test the new codes for a wide range of atmospheric conditions, the IPA has been called in parallel with the new codes in the prototype CAM. The IPA and the new codes are applied to the same atmospheric conditions at each grid point and at each radiation time step. The IPA is executed in a diagnostic mode, and the shortwave and longwave heating rates computed with IPA do not interact with the rest of the model physics. The instantaneous heating rates, TOA fluxes, and surface fluxes from the IPA and new codes have been accumulated every hour during a 1-yr integration and analyzed.

The distribution of differences in the all-sky TOA and surface longwave fluxes are shown in Fig. 5. The distribution is strongly peaked about 0 W m^{-2}, and the figure illustrates that instantaneous differences between IPA and the new code are generally much less than 1 W m^{-2}. At TOA, the instantaneous longwave fluxes differ by -0.006 ± 0.066 W m^{-2}, and at the surface the instantaneous fluxes differ by -0.005 ± 0.202 W m^{-2}. The errors in the fluxes from the new code are caused by tiny inaccuracies in the absorptivities for adjacent layers (Kiehl et al. 1996) and by the method used for the random-overlap boundary conditions between

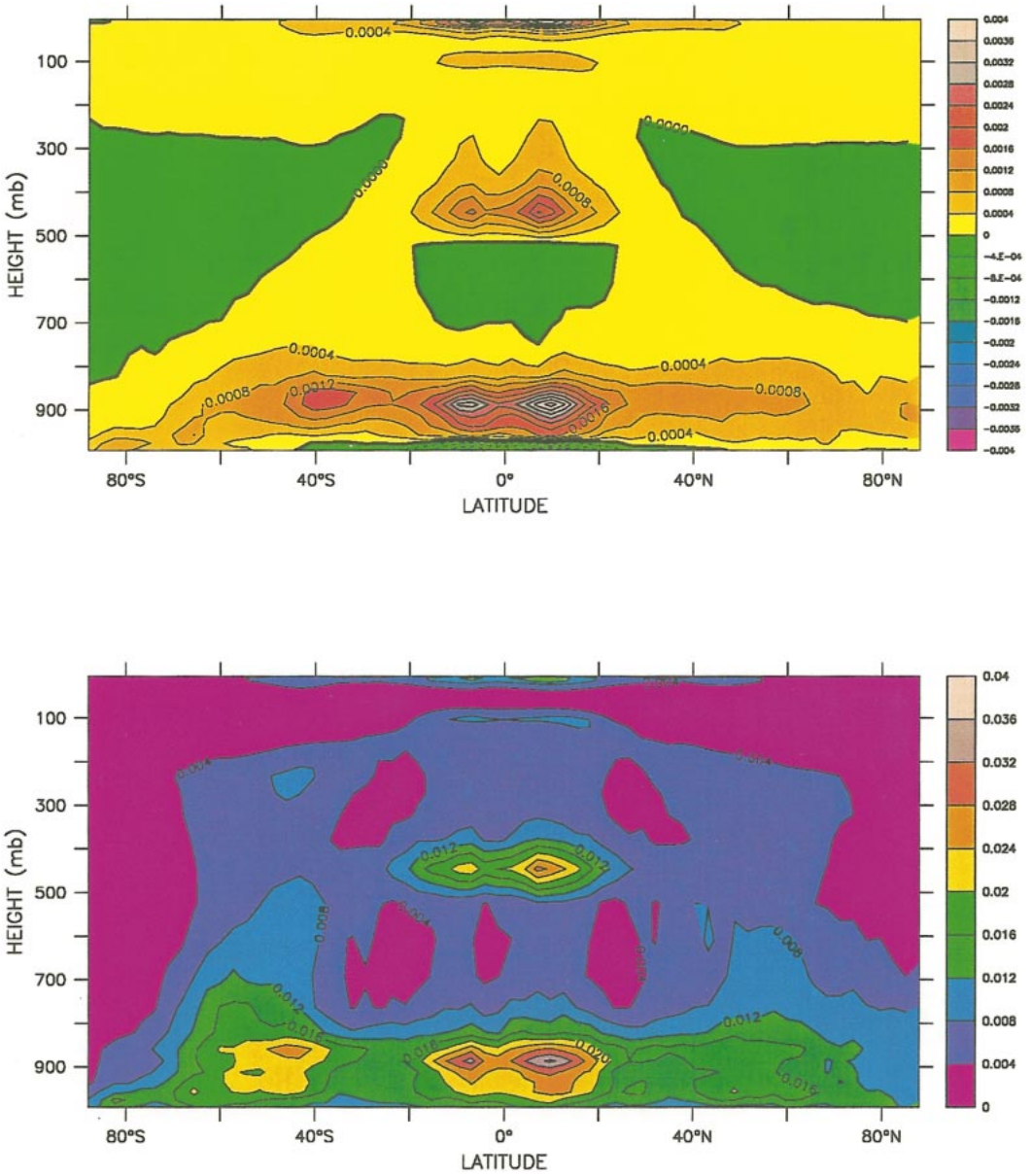

FIG. 8. (a) Zonally averaged mean differences in instantaneous shortwave heat rates Q_{sw} from the IPA and CAM radiation codes; (b) zonally averaged rms differences in instantaneous shortwave heat rates Q_{sw}. The differences are accumulated from a 1-yr integration of CAM at T42 resolution. The heating rates are computed at each radiation time step (1 h^{-1}) at each grid point.

maximally overlapped blocks of clouds (section 3b). The greatest errors in the TOA and surface fluxes encountered during the 1-yr test are -1.5 and -4.1 W m^{-2}, respectively. The mean and rms errors in the instantaneous longwave heating rates are shown in Fig. 6. The largest mean differences are located in the Tropics in two local maxima, one in the upper troposphere and the second in the stratosphere. The differences in the troposphere approach 0.01 K day^{-1}, and the differences in the stratosphere are as large as 0.016 K day^{-1} near the top of the model. Over most of the troposphere, however, the heating rates differ by less than 0.002 K day^{-1}. The errors in the troposphere are at least two orders of magnitude smaller than the annual-mean longwave heating rates at the same locations (section 5). The instantaneous rms differences reach peak values of 0.1 K day^{-1} in the lower troposphere and boundary layer. There is a secondary maximum in the tropical stratosphere where the rms differences are as large as 0.04 K day^{-1}. In the rest of the stratosphere and in the middle and upper troposphere, the instantaneous rms errors are less than 0.03 K day^{-1}.

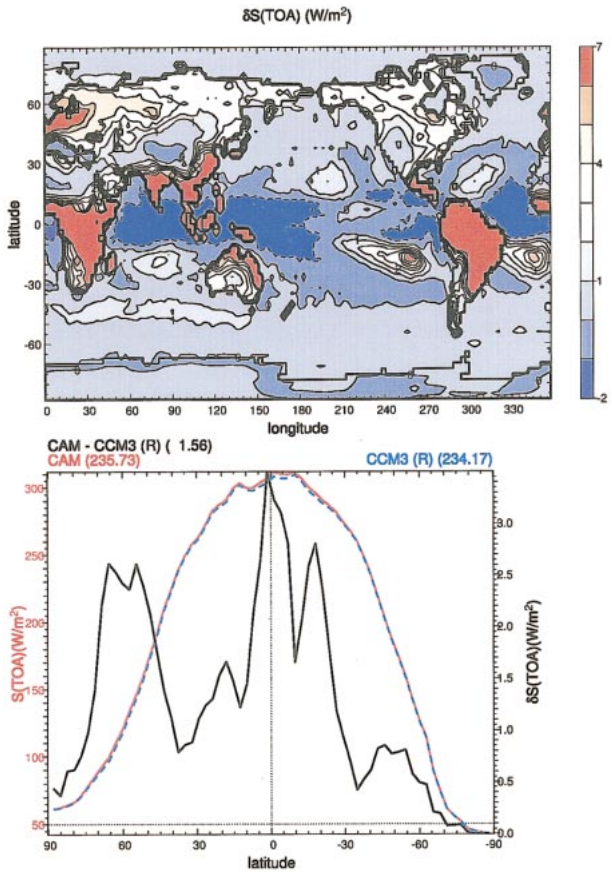

FIG. 9. Gridpoint and zonal-average differences in annual-mean S(TOA) (M/R interactive − R diagnostic). (bottom) Absolute values of fluxes are plotted in red (M/R) and blue (R). Difference is plotted in black.

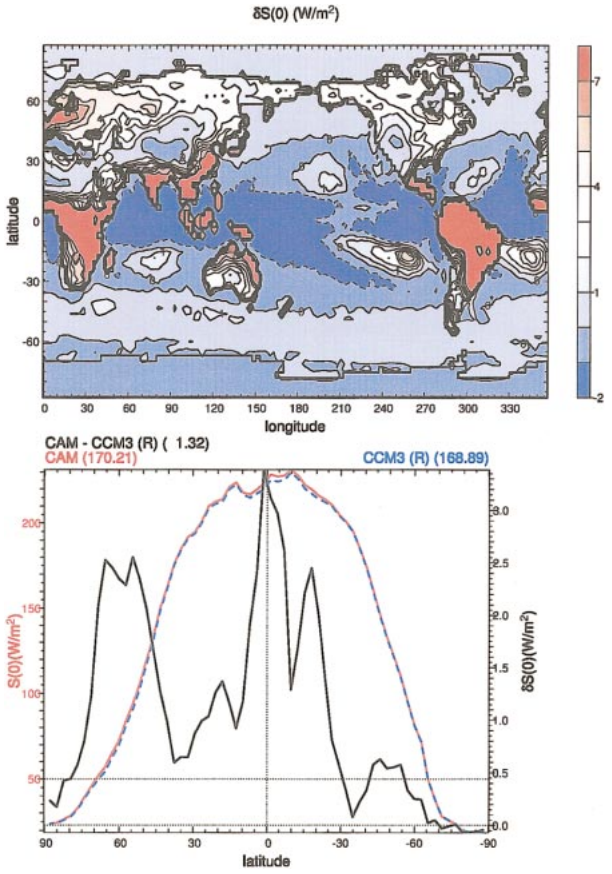

FIG. 10. Gridpoint and zonal-average differences in annual-mean $S(0)$ (M/R interactive − R diagnostic). (bottom) Absolute values of fluxes are plotted in red (M/R) and blue (R). Difference is plotted in black.

The distribution of differences in the all-sky TOA and surface shortwave fluxes are shown in Fig. 7. The mean and rms differences between IPA and the new code are larger for the shortwave than the longwave, although the distributions are still strongly peaked about 0 W m^{-2}. The instantaneous shortwave errors at TOA are -0.202 ± 1.577 W m^{-2}, and the corresponding errors at the surface are -0.229 ± 1.765 W m^{-2}. Ninety-nine percent of the shortwave fluxes from the new codes are within 10 W m^{-2} of the IPA calculations. The errors are introduced by the parameter settings used to accelerate the new shortwave scheme by reducing the number of binary cloud configurations analyzed at each grid point (Table 3). When these parameters are chosen to reproduce the IPA solution as closely as possible, that is, $\tilde{A}_{\min} = 0$ and $N_{c,\max} \gg 1$, the instantaneous differences in the fluxes range from zero to within the roundoff error of the computer hardware. The mean and rms errors in instantaneous shortwave heating rates are shown in Fig. 8. The largest mean and rms errors are located in the Tropics where the zonally averaged annual-mean insolation reaches its peak values. The local maxima in the rms errors are collocated with the local maxima in the mean errors. The greatest mean errors in the tropical troposphere and stratosphere are less than 0.004 K day^{-1}. These errors are at least two orders of magnitude smaller than the annual-mean shortwave heating rates at the same locations in the atmosphere (section 5). The instantaneous rms errors are all less than 0.04 K day^{-1}.

5. Sensitivity of simulated climate to changes in cloud overlap

When the cloud overlap assumption is changed from R to M/R, the effects of clouds on the global annual-mean radiative fluxes are reduced. The reductions in the cloud radiative effects, or ''forcings,'' result from two competing factors. First, the total fractional area of each cloud configuration is smaller under the M/R overlap assumption. Second, the relationships of shortwave albedo and longwave emissivity to condensed water path (CWP) are nonlinear. The cloud albedo and emissivity increase as CWP increases, but the increments in albedo and emissivity per unit change in CWP become smaller as CWP becomes larger (Liou 1992). For plane-parallel clouds, CWP is the vertically integrated mass of con-

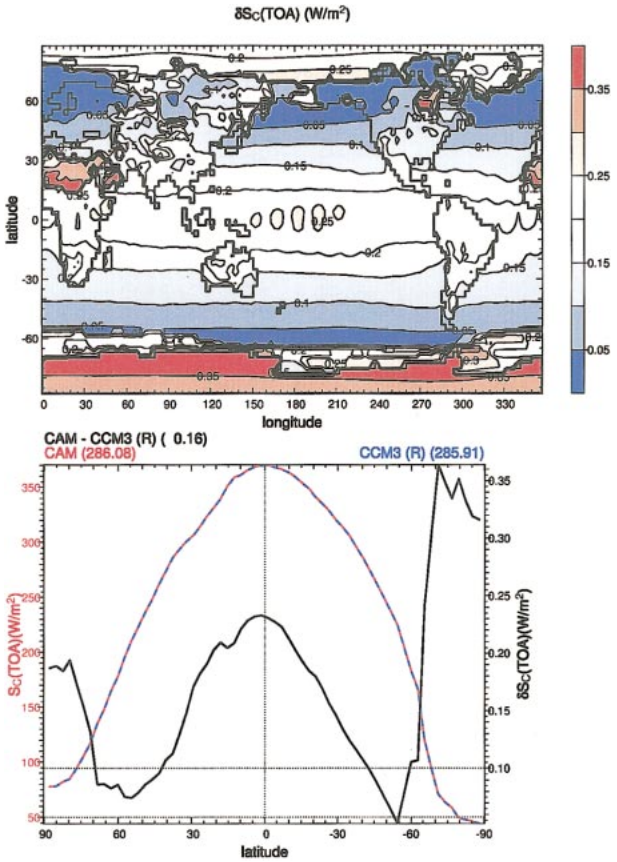

FIG. 11. Gridpoint and zonal-average differences in annual-mean S_c(TOA) from integration of CAM with (M/R interactive − R diagnostic). (bottom) Absolute values of fluxes are plotted in red (M/R) and blue (R). Difference is plotted in black.

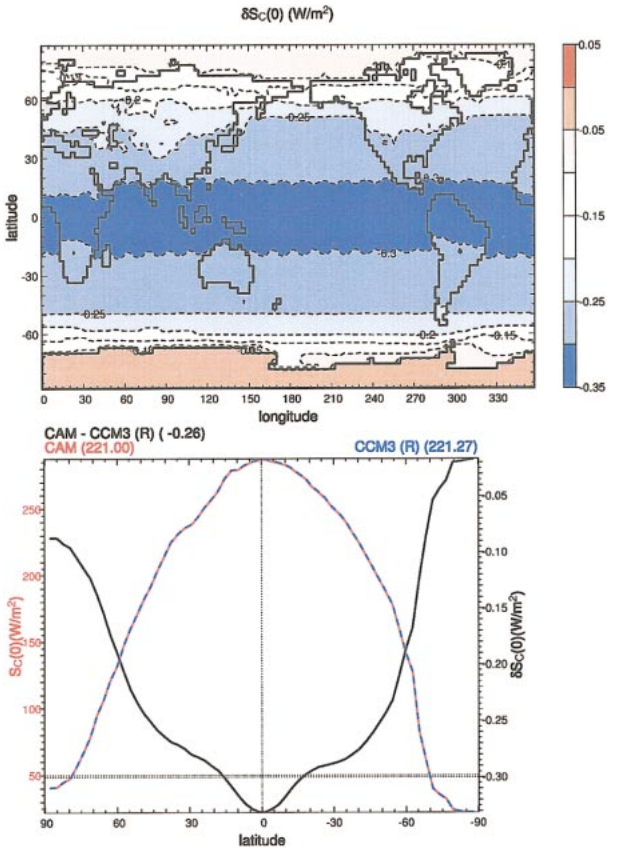

FIG. 12. Gridpoint and zonal-average differences in annual-mean $S_c(0)$ (M/R interactive − R diagnostic). (bottom) Absolute values of fluxes are plotted in red (M/R) and blue (R). Difference is plotted in black.

densed cloud water per unit area. Rearranging randomly overlapped clouds into a maximally overlapped configuration while preserving the total mass of condensed water will generally yield higher cloud albedos and emissivities. The reason is that the CWP will increase in regions where the vertical overlap of clouds increases. However, in most cases the nonlinear increase in cloud radiative properties cannot offset the decrease in the areal coverage. The result is that on average the cloud radiative forcing is reduced as the overlap is changed from R to M/R.

The changes in radiative fluxes and cloud properties resulting from the change in overlap are shown in Table 4. The differences in the first column are calculated from two 5-yr simulations with the prototype CAM running the old and new radiation codes. The only differences between the model configurations in the two simulations are related to the radiative overlap; no retuning has been performed. The global means of these fields from the integration with M/R overlap are shown for comparison in the second column. The differences in the fluxes when the two overlap assumptions interact with the rest of the model physics are denoted by δ_i. The absorbed solar radiation and the net longwave emission increase at both the TOA and the surface. The change in overlap has reduced the planetary albedo by 0.5% and increased the transmission to the surface by 0.4%. The largest relative change is in the surface longwave flux $F(0)$. The prototype of CAM with M/R overlap has a global annual-mean TOA energy balance given by $S(\text{TOA}) - F(\text{TOA}) = -0.03$ W m^{-2}.

The changes in the radiative fluxes result partly from the instantaneous effects of changing cloud overlap and partly from the feedback of these instantaneous effects on the climate simulation. The relative importance of these factors can be determined by calculating the instantaneous radiative effects. Two estimates of the instantaneous changes are given in the third and fourth columns of Table 4 and are denoted by $\delta_{d,1}$ and $\delta_{d,2}$, respectively. The estimates are obtained by comparing fluxes for identical atmospheric states computed with the M/R and R overlap assumptions. In the first estimate, the radiation computed with M/R overlap interacts with the remainder of the model while the radiation computed with R overlap does not. In the second estimate, the radiation with R overlap is interactive while the M/R

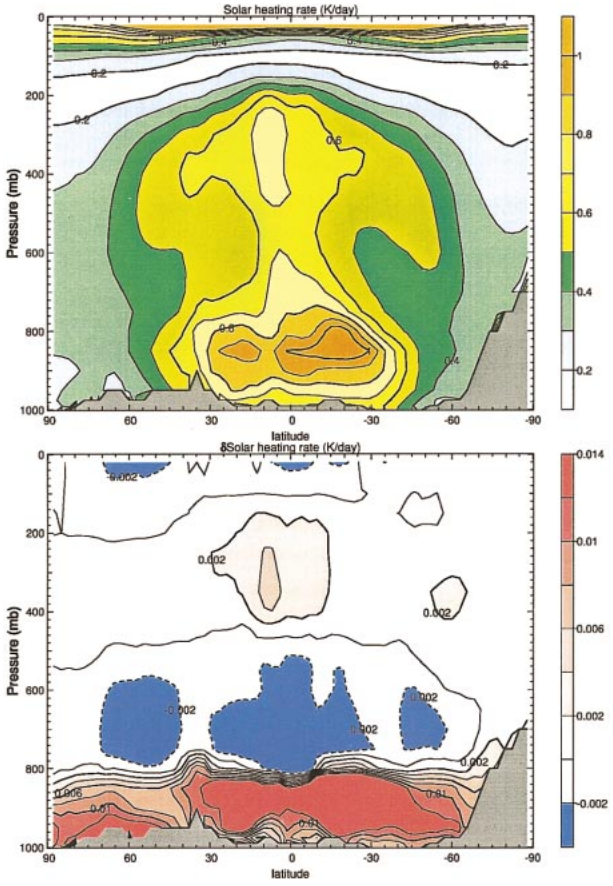

FIG. 13. (a) Zonal-average annual-mean solar heating rate Q_{SW} from integration with M/R interactive; (b) difference in Q_{SW} from integration of CAM with (M/R interactive − R diagnostic).

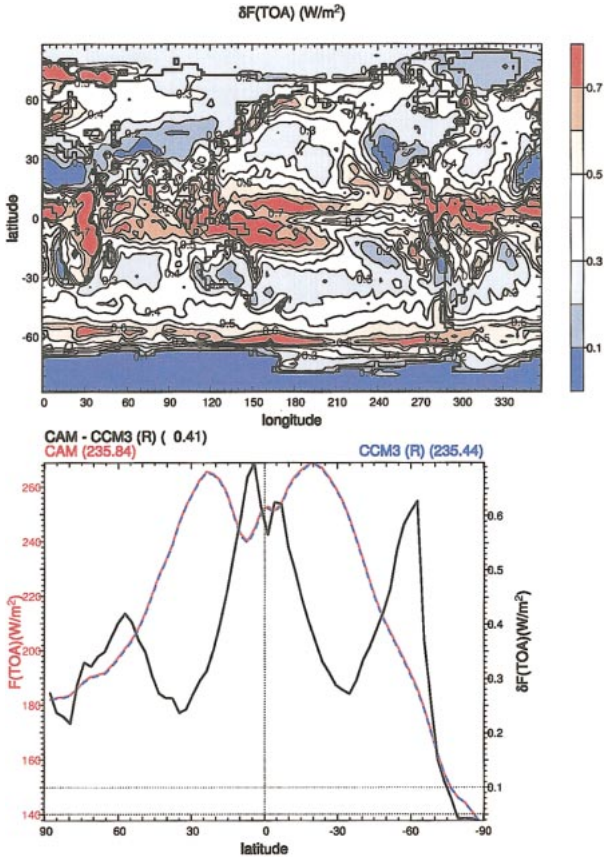

FIG. 14. Gridpoint and zonal-average differences in annual-mean F(TOA) (M/R interactive − R diagnostic). (bottom) Absolute values of fluxes are plotted in red (M/R) and blue (R). Difference is plotted in black.

overlap is diagnostic. These estimates are derived from the same 5-yr integrations used to calculate $\delta_i S$ and $\delta_i F$.

In the shortwave, the instantaneous effects are the dominant components of the flux differences when the overlap is changed from R to M/R. The values of $\delta_{d,1}S$(TOA) and $\delta_{d,2}S$(TOA) differ from $\delta_i S$(TOA) by only 7.7% and 12.8%, respectively. The values of $\delta_{d,1}S(0)$ and $\delta_{d,2}S(0)$ differ from $\delta_i S(0)$ by 1.5% and 7.2%, respectively. If the flux differences are caused primarily by the change in overlap rather than feedbacks on the atmospheric state, then the cloud properties should be very similar in the two integrations. This inference is confirmed by the relatively small changes in cloud distributions and cloud condensate shown in Table 4. The cloud amounts in the lower, middle, and upper troposphere (Table 1) are computed with the M/R overlap assumption regardless of the assumption used in the radiation in order to simplify the comparison. The total cloud amount $\delta_i C_T$, for example, changes by only −0.6% (relative), and the changes in the layer cloud amounts are comparable. The differences in the zonally averaged cloud cover are all less than 2.5% (absolute). The small changes in cloud amount are consistent with the results of similar experiments in the European Centre for Medium-Range Forecasts (ECMWF) model (Morcrette and Jakob 2000). The liquid water path decreases by −0.13% and the ice water path increases by 1.3% when the overlap is switched from R to M/R. In the longwave, the variation in surface flux is again dominated by instantaneous effects. The value of $\delta_i F(0)$ differs from $\delta_{d,1}F(0)$ and $\delta_{d,2}F(0)$ by −13% and −19%, respectively. There is some evidence of feedback in the TOA longwave flux since $\delta_i F$(TOA) is 2.3 times larger than either $\delta_{d,1}F$(TOA) or $\delta_{d,2}F$(TOA). The change in the global outgoing longwave radiation associated with the feedback is approximately 0.5 W m^{-2}.

The gridpoint and zonal-average change $\delta_{d,1}S$(TOA) in TOA solar flux are shown in Fig. 9. The largest differences of 7 W m^{-2} are associated with tropical and subtropical land surfaces, although there are changes of up to 5 W m^{-2} in oceanic cloud systems south of the intertropical convergence zone (ITCZ). The zonal-mean $\delta_{d,1}S$(TOA) is positive at all latitudes and reaches peak values of 3.5 W m^{-2} in the Tropics with secondary maxima over northern continental areas. This plot shows that the net absorbed solar flux has increased at all lat-

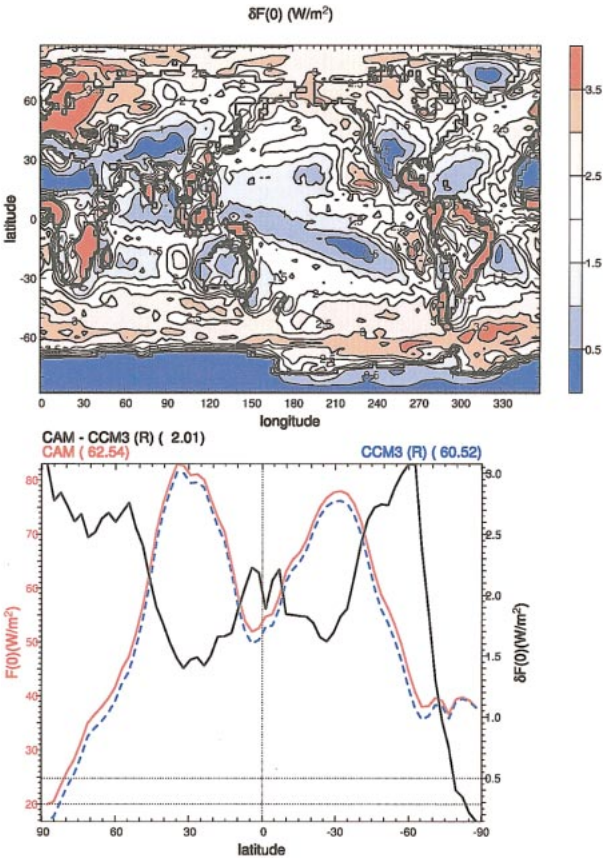

FIG. 15. Gridpoint and zonal-average differences in annual-mean $F(0)$ (M/R interactive − R diagnostic). (bottom) Absolute values of fluxes are plotted in red (M/R) and blue (R). Difference is plotted in black.

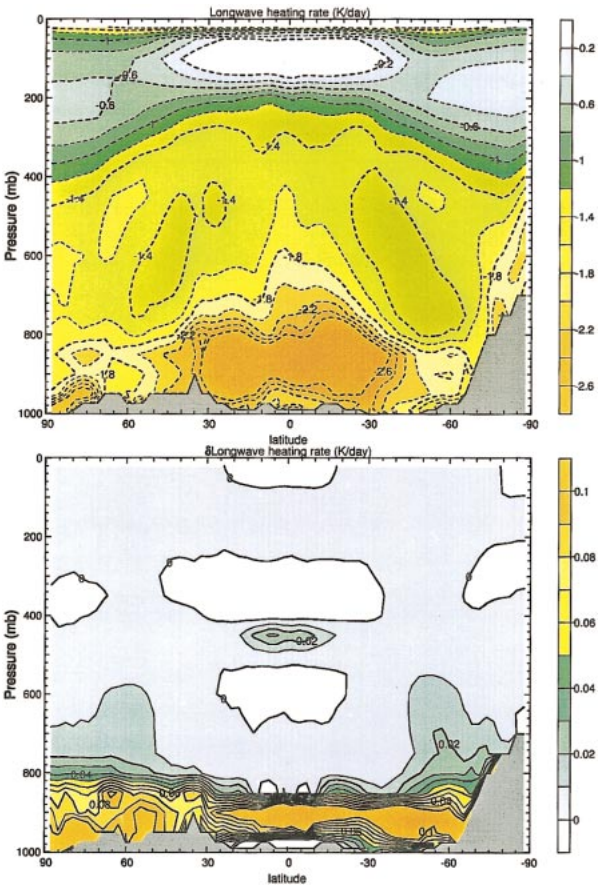

FIG. 16. (a) Zonal-average annual-mean longwave heating rate Q_{LW} from integration with M/R interactive; (b) difference in Q_{LW} from integration of CAM with (M/R interactive − R diagnostic).

itudes due to the change in overlap assumption. The change $\delta_{d,1}S(0)$ plotted in Fig. 10 is very similar in its spatial pattern and magnitude. This is expected since the TOA and surface solar fluxes are strongly correlated. The zonal-mean surface insolation increases at all latitudes by as much as 3.5 W m^{-2}. The clear-sky solar fluxes also change, although the differences are not related to the switch in cloud overlap assumption. In the new parameterizations, the clear-sky fluxes are computed at the full vertical resolution of the model instead of the reduced resolution adopted in CCM3 for computational speed. The TOA clear-sky flux S_c(TOA) increases at all latitudes by up to 0.4 W m^{-2} (Fig. 11), and the surface clear-sky flux $S_c(0)$ decreases at all latitudes by up to 0.35 W m^{-2} (Fig. 12). The zonally symmetric patterns and meridional gradients in $\delta_{d,1}S_c$(TOA) and $\delta_{d,1}S_c(0)$ are related to the zonal symmetry and meridional gradient in TOA solar insolation. The largest changes in the all-sky solar heating rates (Fig. 13) occur in the lower troposphere with peak values of 0.014 K day^{-1}. The heating rates increase in this region of the atmosphere because more solar radiation can penetrate to lower layers with the new overlap assumption. The magnitude of the differences in Q_{SW} in the middle and upper troposphere are generally less than 0.002 K day^{-1}. The fact that the instantaneous differences $\delta_{d,1}Q_{SW}$ and $\delta_{d,1}Q_{LW}$ (shown below) are roughly two orders of magnitude smaller than the annual-mean Q_{SW} and Q_{LW} explains why the climate feedbacks related to cloud overlap are not significant in CAM. In an uncoupled model, the response of the atmosphere to variation in cloud overlap is dictated entirely by the resulting changes in radiative heating rates. If the changes in the heating rates are relatively small, then the response of the simulated climate should also be relatively insignificant. In the integrations of CAM shown here, the atmosphere is coupled to an active land surface model. The response of the land model to the increase in tropical insolation (Fig. 10) is evidently not sufficiently large to change these conclusions.

The principal differences in the TOA longwave flux $\delta_{d,1}F$(TOA) are associated with the ITCZ and the polar fronts at high latitudes (Fig. 14). The differences in these regions of deep cloud systems reach peak values of 0.8 W m^{-2}. The change in overlap from R to M/R increases the outgoing longwave radiation at all latitudes as ex-

pected. In contrast to the shortwave, the effects of clouds on the surface longwave flux are nearly decoupled from the effects at TOA because of the longwave opacity of the atmosphere (Harshvardhan et al. 1990). This decoupling is evident in the map of $\delta_{d,1}F(0)$ shown in Fig. 15. Some of the largest changes in $F(0)$ occur in the oceanic stratus cloud regions on the east coasts of North and South America, Africa, and Australia. There are also significant differences in the polar fronts for both hemispheres. The value of $F(0)$ increases at all latitudes when the overlap is changed from R to M/R. The downward longwave radiation from clouds generally decreases $F(0)$ because clouds are in local thermodynamic equilibrium with the surrounding atmosphere and the tropospheric lapse rate is usually negative. When the effective cloud area is decreased by switching from R to M/R overlap, the cloud radiative effects are reduced and therefore $F(0)$ is increased. As in the shortwave, the largest changes in the longwave heating rate occur in the lower troposphere. The cooling of the lowest layers in the model is reduced by approximately 0.1 K day^{-1} (Fig. 16). The differences in the rest of the troposphere and the stratosphere are less than 0.02 K day^{-1}. The main effect from changing the overlap assumption is to reduce the divergence of longwave flux in the lowest 200 mb of the atmosphere.

The results in Table 4 show that the CAM is relatively insensitive to changes in cloud overlap in the calculation of radiative fluxes. However, this finding does not necessarily apply to other general circulation models (e.g., Morcrette and Jakob 2000).

6. Computational performance of the new parameterizations

The additional flexibility of the new radiative parameterizations increases the computational cost of the CAM. The effects of the new codes on the storage requirements and execution time have been evaluated on distributed-memory scalar-arithmetic machines. These have replaced vector-arithmetic computers as the main platforms for executing CAM. The amount of computer memory has been evaluated for the CAM running at T42 spectral truncation with 30 vertical levels and the old and new radiative parameterizations. The introduction of the new overlap treatment requires 1.2% more memory than the model including the previous random-overlap codes. The increase in the physical, or ''wall clock,'' time required to run CAM on a multiprocessing computer is given in Table 5. The time required to run the model grows by up to 22%, although this increase is probably an upper bound. The additional execution time is smaller when the model is run with a reduced grid (Williamson and Rosinski 2000), and it is expected to be smaller with finer-grained decompositions of the computational grid.

As shown in Table 6, most of the increased execution time is associated with the shortwave calculation. The cost of the new shortwave code (on a multiprocessing system) is approximately double that of the original scheme. The actual number of operations increases by 45%–50% relative to the old code. The new code solves the δ-Eddington equations at full vertical resolution for clear-sky and all-sky conditions. In the previous code, the all-sky calculation is performed at full resolution while the clear-sky calculation is based upon a two-layer representation of the atmosphere. This difference alone suggests that the new code should be at least twice as computationally expensive as the old code. The fact that the execution time increases by a factor slightly greater than 2 indicates that the additional complexity of the all-sky calculation has little impact on the computational cost. The most commonly used methods for treating cloud overlap in shortwave calculations (e.g., Morcrette and Fouquart 1986, and Chou et al. 1998) also require a separate calculation of clear-sky and cloudy-sky radiative properties. Compared to the present method, these schemes would incur similar computational costs but provide considerably lower accuracy in instantaneous fluxes and heating rates. The cost of the longwave code is nearly identical to that of the original random-overlap version. The reason is that over 99% of the computational cost of the original code is related to the calculation of clear-sky radiative properties. Even though the cost of the new cloudy-sky calculation is approximately 8 times larger than the previous cloudy-sky calculation, the cost of the complete longwave calculation (both in the number of operations and in wall clock time) increases by only 3%. This is comparable to the cost for the approximation to longwave overlap in the current version of the ECMWF model (Raisanen 1998). The combined cost of the radiation calculations increases by 31%.

The new codes also increase the load imbalance between processors as shown in Table 7. The variability can be characterized by the ratio of the maximum execution time on any processor to the mean execution time calculated across all processors. On a multiprocessing system, the CAM has several synchronization points for data communication between processors. When a synchronization point is encountered, all calculations up to that point must be complete before proceeding. Processors with a lighter workload that reach the synchronization point first have to wait until all the other processors reach the same point. Therefore, the rate of execution is determined by the rate of the slowest components. In the current version of the CAM, the calculations are divided among the processors by latitude. The variability is only 5% for the longwave because similar calculations have to be performed regardless of latitude, season, or hour of day. In addition, since the cost of the longwave is dominated by the clear-sky calculations, regional variations in cloud distributions have little effect on the variability. However, the variability for the shortwave calculations is significant even for the original code. The greater variability for the

shortwave is related to the seasonal differences in solar insolation between the two hemispheres. The reasons are that the shortwave calculation is performed only when a grid box is illuminated and the length of day has a large seasonal variation. This measure of variability is quite sensitive to the partitioning of the CAM among processors and to the machine architecture, and therefore the performance of CAM on other machines may vary.

7. Conclusions and future work

New parameterizations of vertical cloud overlap have been developed for radiative calculations in GCMs. These methods have been implemented in the NCAR Community Atmospheric Model, the successor to the NCAR CCM. The parameterizations can calculate the all-sky shortwave and longwave fluxes for random overlap, maximum overlap, or an arbitrary combination of maximum and random overlap. While in many existing methods the overlap assumptions are implemented directly in the code, in the present approach the overlap is specified by two quantities input to the radiative calculations. These quantities fix the number of maximum-overlap regions and the locations of the random-overlap boundaries separating them at each grid point. If necessary, the type of cloud overlap could change from one grid point or time step to the next. In CAM, the vertical cloud overlap is maximum/random with maximum overlap between adjacent clouds and random overlap between blocks of clouds separated by clear sky. This type of maximum/random overlap is consistent with observational analyses of cloud distributions.

The shortwave fluxes are calculated by converting a vertical profile of cloud amount into a set of equivalent binary cloud configurations. The radiative transfer equations are solved explicitly for each binary configuration. It has long been assumed that this explicit approach would be too computationally expensive for GCMs, and a variety of approximate techniques have been developed in its place. However, the computational performance of the new parameterizations is comparable to that of several widely used approximations. The performance is achieved in part by eliminating redundant calculations and by omitting cloud configurations with small surface areas from the calculations. It should be noted that the computational cost of the new methods can change as the overlap assumption is changed, and in fact the cost of the shortwave calculations would increase significantly for random overlap. This is one disadvantage of the explicit technique relative to the earlier approximations, which were designed to have nearly constant performance regardless of the type of overlap.

The principal advantage of the new techniques is the very accurate treatment of overlap between plane-parallel homogeneous clouds. The accuracy has been determined by comparing the fluxes and heating rates from the new methods against the same quantities calculated with the IPA. The errors in the new parameterizations relative to IPA have been examined over a wide range of atmospheric conditions. The errors are calculated using hourly instantaneous fluxes and heating rates from a 1-yr integration of CAM. The mean errors in the fluxes are much less than 1 W m^{-2}, and the errors in the tropospheric heating rates are less than 0.01 K day^{-1}. These error estimates do not include systematic biases related to the treatment of radiatively active constituents, the two-stream approximations to the radiative transfer equations, or the omission of cloud inhomogeneities and three-dimensional geometry.

The new parameterizations are one of several improvements in the physical parameterizations planned for CAM. The generalization of cloud overlap may be extended to other cloud processes, in particular the treatment of cloud precipitation and evaporation. This would ensure that the assumptions regarding overlap are consistent among all the parameterizations of cloud physics. The treatment of infrared absorption by water vapor may also be improved by updating the absorptivity–emissivity formulation using line-by-line calculations or by replacing the absorptivity–emissivity calculations with the correlated-*k* method. Once these improvements have been implemented, the model cloud fields and fluxes should be compared against the latest satellite observations and field data. The evaluation of CAM using the new generation of satellites devoted to cloud measurements will be used to guide further development of the model.

Acknowledgments. The author would like to thank B. Briegleb (NCAR), J. Hack (NCAR), J. Kiehl (NCAR), V. Ramanathan (UCSD), and A. Slingo (U.K. Hadley Centre) for discussions regarding the treatment of cloud overlap. The author would also like to acknowledge J. Truesdale (NCAR) for his invaluable assistance in developing the new overlap codes. J. Truesdale was supported in part by the U.S. Department of Energy Climate Change Prediction Program. The comments of two anonymous reviewers and J.-J. Morcrette have been instrumental in improving the manuscript. Computational resources were provided by NCAR.

APPENDIX

Derivation of the Longwave Solution

The simplification of the longwave solution will be demonstrated for the downwelling fluxes. For a region j, the boundary conditions are

$$F^{\downarrow}[k_1, \ldots, k_{j-1}](i_{j,\min})$$

$$= \text{downwelling flux at upper boundary of region } j \text{ for the binary cloud configuration } \tilde{C}[k_1, \ldots, k_{j-1}] \text{ above the boundary,} \quad \text{(A1)}$$

$\overline{F}^{\downarrow}(i_{j,\min})$

= mean downwelling flux at upper boundary of region j

$$= \sum_{k_1=1}^{n_1+1} \cdots \sum_{k_{j-1}=1}^{n_{j-1}+1} \tilde{A}[k_1, \ldots, k_{j-1}] \times F^{\downarrow}[k_1, \ldots, k_{j-1}](i_{j,\min}), \quad \text{(A2)}$$

where

$$\tilde{C}[k_1, \ldots, k_{j-1}](i) = \sum_{j'=1}^{j-1} \tilde{C}_{j',k_{j'}}(i), \quad \text{and} \quad \text{(A3)}$$

$$\tilde{A}[k_1, \ldots, k_{j-1}] = \prod_{j'=1}^{j-1} \tilde{A}_{j',k_{j'}}. \quad \text{(A4)}$$

The factor $\tilde{A}[k_1, \ldots, k_{j-1}]$ in Eq. (A2) is the area occupied by a configuration $\tilde{C}[k_1, \ldots, k_{j-1}]$ based upon random overlap between regions. The collection of all configurations $\tilde{C}[k_1, \ldots, k_{j-1}]$ fills the grid box:

$$\sum_{k_1=1}^{n_1+1} \cdots \sum_{k_{j-1}=1}^{n_{j-1}+1} \tilde{A}[k_1, \ldots, k_{j-1}] = 1. \quad \text{(A5)}$$

For a layer i within the region j, let $F^{\downarrow}[k_1, \ldots, k_j](i)$ represent the downward flux for the binary cloud configuration $\tilde{C}_{j,k_j}$ and boundary condition $F^{\downarrow}[k_1, \ldots, k_{j-1}](i_{j,\min})$. The mean downwelling longwave flux at layer i for configuration $\tilde{C}_{j,k_j}$ is

$$\overline{F}[k_j]^{\downarrow}(i) = \sum_{k_1=1}^{n_1+1} \cdots \sum_{k_{j-1}=1}^{n_{j-1}+1} \tilde{A}[k_1, \ldots, k_{j-1}] F^{\downarrow}[k_1, \ldots, k_j](i). \quad \text{(A6)}$$

Here $\tilde{A}[k_1, \ldots, k_{j-1}]$ is the conditional probability that $\tilde{C}[k_1, \ldots, k_{j-1}]$ overlaps $\tilde{C}_{j,k_j}$ on the upper boundary of region j. Because the solution to the longwave equations is linear in the boundary condition,

$$F^{\downarrow}[k_1, \ldots, k_j](i) = a_j(i, k_j) + b_j(i, k_j) F^{\downarrow}[k_1, \ldots, k_{j-1}](i_{j,\min}), \quad \text{(A7)}$$

where $a_j(i, k_j)$ and $b_j(i, k_j)$ depend only upon conditions within region j. Then the mean flux for configuration $\tilde{C}_{j,k_j}$ [Eq. (A6)] can be rewritten using Eqs. (A2), (A5), and (A7) in the form

$$\overline{F}[k_j]^{\downarrow}(i) = a_j(i, k_j) \sum_{k_1=1}^{n_1+1} \cdots \sum_{k_{j-1}=1}^{n_{j-1}+1} \tilde{A}[k_1, \ldots, k_{j-1}] + b_j(i, k_j) \sum_{k_1=1}^{n_1+1} \cdots \sum_{k_{j-1}=1}^{n_{j-1}+1} \times \tilde{A}[k_1, \ldots, k_{j-1}] F^{\downarrow}[k_1, \ldots, k_{j-1}](i_{j,\min}) \quad \text{(A8)}$$

$$= a_j(i, k_j) + b_j(i, k_j) \overline{F}^{\downarrow}(i_{j,\min}). \quad \text{(A9)}$$

Therefore $\overline{F}[k_j]^{\downarrow}(i)$ can be calculated from a single solution of the longwave radiative equations with $\overline{F}^{\downarrow}(i_{j,\min})$ as the boundary condition.

REFERENCES

Barker, H. W., 1996: A parameterization for computing grid-averaged solar fluxes for inhomogeneous marine boundary layer clouds. Part I: Methodology and homogeneous biases. *J. Atmos. Sci.,* **53,** 2289–2303.

——, and B. A. Wielicki, 1997: Parameterizing grid-averaged longwave fluxes for inhomogeneous marine boundary layer clouds. *J. Atmos. Sci.,* **54,** 2785–2798.

Bergman, J. W., and H. H. Hendon, 1998: Calculating monthly radiative fluxes and heating rates from monthly cloud observations. *J. Atmos. Sci.,* **55,** 3471–3491.

Briegleb, B. P., 1992: Delta-Eddington approximation for solar radiation in the NCAR Community Climate Model. *J. Geophys. Res.,* **97,** 7603–7612.

Cahalan, R. F., W. Ridgway, W. J. Wiscombe, S. Gollmer, and Harshvardhan, 1994: Independent pixel and Monte Carlo estimates of stratocumulus albedo. *J. Atmos. Sci.,* **51,** 3776–3790.

Chou, M.-D., M. J. Suarez, C.-H. Ho, M. M.-H. Yan, and K.-T. Lee, 1998: Parameterization of cloud overlapping and shortwave single-scattering properties for use in general circulation and cloud ensemble models. *J. Climate,* **11,** 202–214.

Fouquart, Y., 1988: *Physically-Based Modelling and Simulation of Climate and Climate Change.* Vol. 1, *Radiative Transfer in Climate Modeling,* M. E. Schlesinger, Ed., Kluwer Academic, 223–283.

——, and B. Bonnel, 1980: Computation of solar heating of the Earth's atmosphere: A new parameterization. *Beitr. Phys. Atmos.,* **53,** 35–62.

Geleyn, J.-F., and A. Hollingsworth, 1979: An economical analytical method for the computation of the interaction between scattering and line absorption of radiation. *Beitr. Phys. Atmos.,* **52,** 1–16.

——, A. Hense, and H.-J. Preuss, 1982: A comparison of model generated radiation fields with satellite measurements. *Beitr. Phys. Atmos.,* **55,** 253–286.

Goody, R. M., and Y. L. Yung, 1989: *Atmospheric Radiation*. 2d ed. Oxford University Press, 519 pp.

Hack, J. J., 1998: Sensitivity of the simulated climate to a diagnostic formulation for cloud liquid water. *J. Climate,* **11,** 1497–1515.

——, J. T. Kiehl, and J. W. Hurrell, 1998: The hydrologic and thermodynamic characteristics of the NCAR CCM3. *J. Climate,* **11,** 1179–1206.

Harshvardhan, R. Davies, D. A. Randall, and T. G. Corsetti, 1987: A fast radiation parameterization for general circulation models. *J. Geophys. Res.,* **92,** 1009–1016.

——, D. A. Randall, and D. A. Dazlich, 1990: Relationship between the longwave cloud radiative forcing at the surface and the top of the atmosphere. *J. Climate,* **3,** 1435–1443.

Haskins, R. D., T. P. Barnett, M. M. Tyree, and E. Roeckner, 1995: Comparison of cloud fields from AGCM, in situ, and satellite measurements. *J. Geophys. Res.,* **100,** 1367–1378.

Hense, A., M. Kerschgens, and E. Raschke, 1982: An economical method for computing radiative transfer in circulation models. *Quart. J. Roy. Meteor. Soc.,* **108,** 231–252.

Hogan, R. J., and A. J. Illingworth, 2000: Deriving cloud statistics from radar. *Quart. J. Roy. Meteor. Soc.,* **126,** 2903–2909.

Hunt, G. E., 1971: A review of computational techniques for analysing the transfer of radiation through a model cloudy atmosphere. *J. Quant. Spectrosc. Radiat. Transfer,* **11,** 655–690.

Hurrell, J. W., J. J. Hack, B. A. Boville, D. L. Williamson, and J. T. Kiehl, 1998: The dynamical simulation of the NCAR Community Climate Model Version 3 (CCM3). *J. Climate,* **11,** 1207–1236.

Jakob, C., and S. A. Klein, 1999: The role of vertically varying cloud fraction in the parameterization of microphysical processes in the ECMWF model. *Quart. J. Roy. Meteor. Soc.,* **125,** 941–965.

——, and ——, 2000: A parameterization of the effects of cloud and precipitation overlap for use in general circulation models. *Quart. J. Roy. Meteor. Soc.,* **126,** 2525–2544.

Kiehl, J. T., J. J. Hack, G. Bonan, B. Boville, B. Briegleb, D. Williamson, and P. Rasch, 1996: Description of the NCAR Community Climate Model (CCM3). NCAR Tech. Rep. NCAR/TN-420+STR, National Center for Atmospheric Research, Boulder, CO, 152 pp.

——, ——, ——, ——, D. L. Williamson, and P. J. Rasch, 1998a: The National Center for Atmospheric Research Community Climate Model: CCM3. *J. Climate,* **11,** 1131–1149.

——, ——, and J. W. Hurrell, 1998b: The energy budget of the NCAR Community Climate Model: CCM3. *J. Climate,* **11,** 1151–1178.

Lacis, A. A., and J. E. Hansen, 1974: A parameterization for the absorption of solar radiation in the earth's atmosphere. *J. Atmos. Sci.,* **31,** 118–133.

——, and V. Oinas, 1991: A description of the correlated k distribution method for modeling nongray gaseous absorption, thermal emission, and multiple scattering in vertically inhomogeneous atmospheres. *J. Geophys. Res.,* **96,** 9027–9063.

Li, J., 2000: Accounting for overlap of fractional cloud in infrared radiation. *Quart. J. Roy. Meteor. Soc.,* **126,** 3325–3342.

Liang, X. Z., and W. C. Wang, 1997: Cloud overlap effects on general circulation model climate simulations. *J. Geophys. Res.,* **102,** 11 039–11 047.

Lin, S.-J., and R. B. Rood, 1996: Multidimensional flux-form semi-Lagrangian transport schemes. *Mon. Wea. Rev.,* **124,** 2046–2070.

——, and ——, 1997: An explicit flux-form semi-Lagrangian shallow-water model on the sphere. *Quart. J. Roy. Meteor. Soc.,* **123,** 2477–2498.

Liou, K.-N., 1992: *Radiation and Cloud Processes in the Atmosphere*. Oxford University Press, 487 pp.

Manabe, S., and F. Möller, 1961: On the radiative equilibrium and heat balance of the atmosphere. *Mon. Wea. Rev.,* **89,** 503–562.

——, and R. Strickler, 1964: Thermal equilibrium of the atmosphere with a convective adjustment. *J. Atmos. Sci.,* **21,** 361–385.

Morcrette, J.-J., and J.-F. Geleyn, 1985: On the influence of different radiation parameterizations on model-generated radiation fields. *Quart. J. Roy. Meteor. Soc.,* **111,** 565–585.

——, and Y. Fouquart, 1986: The overlapping of cloud layers in shortwave radiation parameterizations. *J. Atmos. Sci.,* **43,** 321–328.

——, and C. Jakob, 2000: The response of the ECMWF model to changes in the cloud overlap assumption. *Mon. Wea. Rev.,* **128,** 1707–1732.

Phillips, T. J., 1994: A summary documentation of the AMIP models. PCMDI Tech. Rep. 18, Lawrence Livermore National Laboratory, Livermore, CA, 343 pp.

Raisanen, P., 1998: Effective longwave cloud fraction and maximum-random overlap of clouds: A problem and a solution. *Mon. Wea. Rev.,* **126,** 3336–3340.

Ramanathan, V., and P. Downey, 1986: A nonisothermal emissivity and absorptivity formulation for water vapor. *J. Geophys. Res.,* **91,** 8649–8666.

Rasch, P. J., and J. E. Kristjánsson, 1998: A comparison of the CCM3 model climate using diagnosed and predicted condensate parameterizations. *J. Climate,* **11,** 1587–1614.

Stephens, G. L., 1984: The parameterization of radiation for numerical weather prediction and climate studies. *Mon. Wea. Rev.,* **112,** 826–867.

Stubenrauch, C. J., A. D. Del Genio, and W. B. Rossow, 1997: Implementation of subgrid cloud vertical structure inside a GCM and its effect on the longwave budget. *J. Climate,* **10,** 273–287.

Tian, L., and J. A. Curry, 1989: Cloud overlap statistics. *J. Geophys. Res.,* **94,** 9925–9935.

Wang, J., W. B. Rossow, and Y. Zhang, 2000: Cloud vertical structure and its variations from a 20-yr global rawinsonde dataset. *J. Climate,* **13,** 3041–3056.

Washington, W. M., and D. L. Williamson, 1977: A description of the NCAR global circulation models. *General Circulation Models of the Atmosphere,* J. Chang, Ed., Vol. 17, *Methods in Computational Physics,* Academic Press, 111–172.

Williamson, D., 1999: Redesign of the NCAR CCM: Algorithms and code. *Parallel Computing in Meteorology and Oceanography: Extended Abstracts, 11th Annual BMRC Modelling Workshop,* Melbourne, Australia, BMRC Research Rep. 75, 67–72.

——, and P. J. Rasch, 1989: Two-dimensional semi-Lagrangian transport with shape preserving interpolation. *Mon. Wea. Rev.,* **117,** 102–129.

——, and J. M. Rosinski, 2000: Accuracy of reduced grid calculations. *Quart. J. Roy. Meteor. Soc.,* **126,** 1619–1640.

——, J. T. Kiehl, V. Ramanathan, R. E. Dickinson, and J. J. Hack, 1987: Description of NCAR Community Climate Model (CCM1). NCAR Tech. Rep. NCAR/TN-285+STR, 112 pp.

Zdunkowski, W. G., W.-G. Panhans, R. M. Welch, and G. J. Korb, 1982: A radiation scheme for circulation and climate models. *Contrib. Atmos. Phys.,* **55,** 215–238.

Zhang, G. J., and N. A. McFarlane, 1995: Sensitivity of climate simulations to the parameterization of cumulus convection in the Canadian Climate Centre general circulation model. *Atmos.–Ocean,* **33,** 407–446.

——, J. T. Kiehl, and P. J. Rasch, 1998: Response of climate simulation to a new convective parameterization in the National Center for Atmospheric Research Community Model (CCM3). *J. Climate,* **11,** 2097–2115.

Zuidema, P., and K. F. Evans, 1998: On the validity of the independent pixel approximation for boundary layer clouds observed during ASTEX. *J. Geophys. Res.,* **103,** 6059–6074.